Journal of Hydrology 632 (2024) 130899

Contents lists available at ScienceDirect

Journal of Hydrology

journal homepage: www.elsevier.com/locate/jhydrol

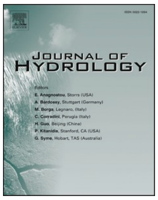

Research papers

Multiple-point geostatistics-based spatial downscaling of heavy rainfall fields

Wenyue Zou [a,*], Guanghui Hu [a,c], Pau Wiersma [a], Shuiqing Yin [b], Yuanyuan Xiao [b],
Grégoire Mariethoz [a], Nadav Peleg [a]

[a] *Institute of Earth Surface Dynamics, University of Lausanne, Lausanne 1015, Switzerland*
[b] *State Key Laboratory of Earth Surface Processes and Resource Ecology, Faculty of Geographical Science, Beijing Normal University, Beijing 100875, China*
[c] *College of Geography and Environmental Sciences, Zhejiang Normal University, Jinhua 321004, China*

ARTICLE INFO

Keywords:
Downscaling rainfall
MPS model
Hourly gridded rainfall
Heavy rainfall
Rainfall spatial structure

ABSTRACT

High-resolution gridded rainfall products at sub-daily and 10^0 km scales are required for hydrological applications in mountainous and urban catchments. As most catchments are ungauged, gridded rainfall data are often obtained through remote sensing. However, their spatial resolution is often too coarse (at 10^1 km) and requires to be downscaled to a finer resolution. The challenge is not only to downscale the rainfall intensity to a finer scale by considering areal reduction factors, but also the spatial structure of the storm, as both elements are equally important to the assessment of the surface hydrological response. As a result of the lack of training data, the latter is difficult to obtain. Further development of the stochastic multiple-point geostatistics (MPS) framework is presented to downscale long-term satellite-derived gridded rainfall series using only a few years of high-resolution rainfall observations. We demonstrate how the MPS framework can be used to downscale the satellite-derived CMORPH rainfall from 8 to 1 km resolution for 1998–2019, taking the city of Beijing as a case study, with a specific focus on extreme rainfall events. The high-resolution multisource-merged CMPAS dataset (1 km, hourly), available for 2015–2020, is used as the source of the training images. We show that the downscaling framework preserves the observed mean areal rainfall (with a bias of 2 %), reproduces the spatial coefficient of variance (with a similar bias), and also retains extreme rainfall at the 99th percentile (with a bias of 6 %). Furthermore, it adequately reproduces the rainfall spatial structure, preserving the variograms of the rainfall fields. Similarities were also observed comparing the 2- to 30-year return period maps of the downscaled rainfall extreme with ground observations, with half of the stations (10 out of 19) agreeing on the location and intensity of the extreme rainfall for all return periods. The results indicate that our framework downscales rainfall intensities and preserves the spatial structure well, especially for heavy rainfall, even if limited data is available. The proposed approach can be applied to other rainfall datasets and regions.

1. Introduction

High-resolution rainfall data in space and time are required for hydrometeorological, ecological, and environmental applications (Karger et al., 2017). In hydrology, the high spatial variability of rainfall at small scales is shown to have a large impact on the catchment hydrological response, especially when considering extreme rainfall intensities (Peleg et al., 2018; Wright et al., 2013). This is even more pronounced in flood impact studies that are conducted in fast-responding hydrological environments, such as in mountainous (Moraga et al., 2021) and urban areas (Cristiano et al., 2017; Dao et al., 2020; Peleg et al., 2017), for which high space–time resolution in the order of kilometer and (sub-) hourly scales are required (Ochoa-Rodriguez et al., 2015; Zhu et al., 2018).

Even though high-resolution spatial rainfall fields are needed as gridded input into hydrological models, they are not available for most catchments. C- and X-band weather radars can provide estimates of rainfall fields at the required resolution (e.g., Marra and Morin, 2018) but due to their high maintenance level and costs, their deployment is limited to cover large areas (i.e., at continental scale) in the US (Molter et al., 2021), Europe (Huuskonen et al., 2014) and China (Shen et al., 2018). Moreover, many weather radar systems were deployed in the

---

* Corresponding author.
E-mail address: wenyue.zou@unil.ch (W. Zou).

https://doi.org/10.1016/j.jhydrol.2024.130899
Received 11 July 2023; Received in revised form 14 January 2024; Accepted 20 January 2024

recent two decades, hence their time series are usually relatively short and span only a few years. With no other alternative, gridded rainfall data can be obtained from other remote sensing devices (directly or post-processed with ground stations and/or climate models), like the global PERSIANN (Sorooshian et al., 2000) and CMORPH (Joyce et al., 2004) products. Despite the fact that these products usually record rainfall for longer periods than weather radars, they are still limited to data collected during the past two or three decades at most. While the hourly to the sub-hourly temporal resolution of these products is sufficient for most hydrological applications, their spatial resolution is often too coarse (10^1 km) and requires downscaling (e.g., to 10^0 km resolution).

There are many different methods for downscaling rainfall (see e.g., the review paper by Abdollahipour et al., 2022), from simply applying a correction based on an areal reduction factor (Thorndahl et al., 2019) to a setup of a complex stochastic framework that preserves the rainfall space–time structure between scales (Peleg et al., 2020). Roughly, downscaling methods can be divided into two groups: (i) simple downscaling models that are light in training-data requirements and can satisfactorily downscale the rainfall intensity but without explicitly adjusting the rainfall spatial structure; and (ii) more complex downscaling models that can also account for the adjustment in rainfall fields when moving between scales but require considerable data as input for the model training. Using the latter methods is recommended, but training data, i.e., rainfall fields at the required space–time resolution of the desired downscaled product, are often insufficient in length, thus making these methods challenging to apply. A geostatistical generation method can serve as a solution that will enable downscaling of tens of years of remotely sensed data using limited training data of only several years in length, as further presented below.

Geostatistical generation methods are widely applied to model spatial correlations in geology, remote sensing, and earth surface science (Benoit and Mariethoz, 2017; Gravey and Mariethoz, 2020; Mariethoz et al., 2010; Oriani et al., 2017; Zou et al., 2021). Essentially, these methods statistically learn spatial patterns from given training data and can stochastically produce a new image (i.e., field) or complete missing information in a given image by following the learned spatial correlation and magnitude (Mariethoz and Caers, 2015). One commonly applied approach is variogram-based geostatistical kriging, which explores spatial relations by using exclusive pairs of points to obtain covariance functions (Gribov and Krivoruchko, 2020; Oliver and Webster, 2014). However, the variogram sometimes fails to accurately represent the spatial structure if training data is limited or if the spatial structure is complex (Chen et al., 2021). An alternative approach is multiple-point geostatistics (MPS), which uses more complex structures with higher-order nonparametric statistics, and it can be applied when the training data is extremely limited (Mariethoz et al., 2010; Mariethoz, 2018; Mariethoz and Caers, 2015). MPS was initially developed to model geological features with solid contacts and connected structures (Chen et al., 2018; Cui et al., 2021; MacKie et al., 2020; Yin et al., 2022), but it is also applied in climate and hydrological sciences (Jha et al., 2015; MacKie et al., 2020; Oriani et al., 2014).

Oriani et al. (2017) demonstrated that MPS could simulate small-scale (1 km) daily rainfall fields. Beyond using radar images and station observation as training data, they conditioned the spatial statistics with elevation and showed that the MPS preserved both the temporal and spatial weather patterns. The method was also applied in the context of downscaling of rainfall. Jha et al. (2015) downscaled one year of daily rainfall from 50 km to 10 km based on the Direct Sampling MPS algorithm (Mariethoz et al., 2010) using multivariate training images from the Weather Research and Forecasting (WRF) model. It is apparent from these past studies that the MPS method can be used to downscale rainfall at much finer temporal scales (i.e., minutes to hours) than previously attempted. However, sub-daily rainfall exhibits a more dynamic spatial structure that evolves rapidly in time and space (Muñoz et al., 2018; Peleg and Morin, 2012), making training and capturing it by an MPS-based algorithm a challenging task.

This study aims to develop a spatial downscaling approach that can stochastically downscale rainfall from a coarse-resolution dataset (10^1 km) to high-resolution rainfall fields (at 10^0 km) based on a limited sample of high-resolution training images using the MPS method. As a study case, we demonstrated downscaling hourly rainfall fields from an 8 km to a 1 km resolution in Beijing. Our study specifically focuses on the downscaling potential of heavy rainfall fields due to their risk of triggering pluvial floods in urban and small rural catchments.

2. The MPS model

MPS is a simulation technique that generates or fills missing parts in target images (also called gridded data or fields) while preserving the spatial features of training images. It is possible to use the same or a different data source for the training images, provided the training images contain the required statistical information as the end target. Therefore, the training images do not need to be from the same period as the target images but should statistically reflect the target period. Consequently, MPS can potentially be used as a stochastic downscaling method if the training images are of higher resolution than the target images.

The MPS family consists of different algorithms. The first pixel-based MPS algorithm, ENESIM, was introduced by Guardiano and Srivastava (1993). The ENESIM simulates categorical variables based on all possible matches in training images, which could result in massive computational costs. Another example is the Direct Sampling algorithm, a more advanced and memory-efficient MPS method (Mariethoz et al., 2010). However, this algorithm requires some parameterization on the user's part and is not easy to implement. This has led to a more flexible and easy-to-use MPS method, Quick Sampling (QS), being proposed recently (Gravey and Mariethoz, 2020). This method uses fast Fourier transforms to rapidly compute mismatches and select candidate patterns by decomposing the standard distance metrics as sums of cross-correlation. In this study, the QS algorithm has been further developed to enable rainfall downscaling, and its basic concepts are outlined in the following paragraphs.

The MPS-QS algorithm is illustrated in Fig. 1 with a simplified example. Fig. 1a is the target image, a rainfall field with several missing values; grid values indicate the rainfall intensity in mm h^{-1} and their colors represent high (dark blue) to low (light blue) intensities. Fig. 1b is a training image, with the same dimension and resolution as the target image but from a different time (the process of selecting the most appropriate training image from the image archive is described in Section S1). The algorithm executes the following steps:

1. For the unknown value y in the target image (Fig. 1a), its neighboring known values, e.g., 10, 15, and 18, are marked as conditioning data $N(y)$ ($N = 3$ in this case).
2. Find the similar structures/patterns $N(xi)$ from the training image (Fig. 1b) and compute their distances (similarities) to $N(y)$. Then, rank the patterns by their distance index (sum of squared error, see Gravey and Mariethoz, 2020); a smaller distance indicates more similarity between pattern and conditioning data (Fig. 1c). For example, out of the four patterns A, B, C, and D visible in the training image (Fig. 1b), pattern B is ranked first (Fig. 1c).
3. The patterns to be assigned in the target image are selected by the K-sampling strategy. When the parameter K is equal to 1, the best pattern is selected, and when it is equal to 2, one of the two best patterns is selected (with equal weight). Taking K to be 1.5, as in the example (Fig. 1c), selecting the best pattern will be weighted proportionally, i.e., 67.7 % and 33.3 % for the first- and second-best patterns, respectively.
4. The value from the selected pattern is finally assigned to the unknown y in the target image.

In the example presented in Fig. 1, we use a single training image to

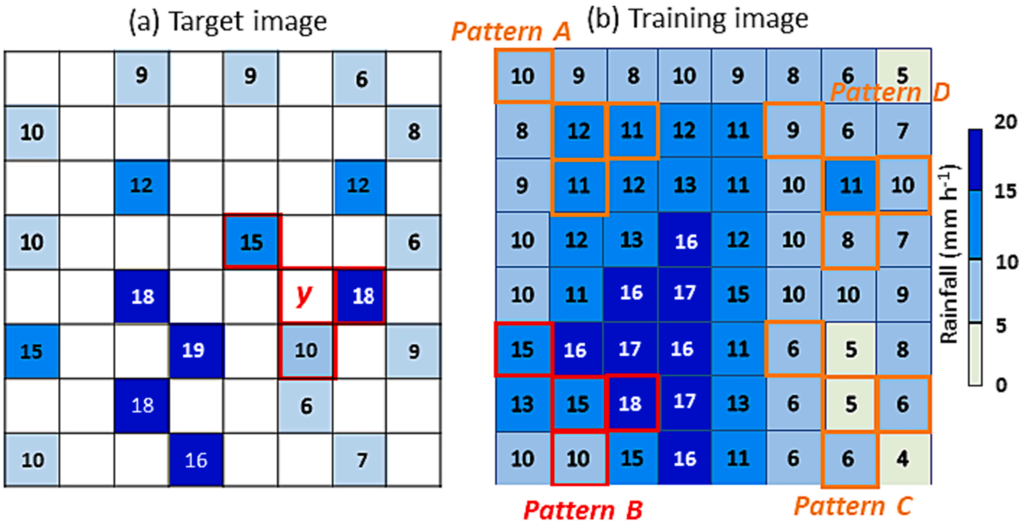
(a) Target image

		9		9		6	
10							8
		12				12	
10				15			6
		18			*y*	18	
15			19		10		9
		18			6		
10			16			7	

(b) Training image

10	9	8	10	9	8	6	5
8	12	11	12	11	9	6	7
9	11	12	13	11	10	11	10
10	12	13	16	12	10	8	7
10	11	16	17	15	10	10	9
15	16	17	16	11	6	5	8
13	15	18	17	13	6	5	6
10	10	15	16	11	6	6	4

(c) K-sampling strategy

Rank	*1*	*2*	*3*	*4*	*...*
Distance	*0*	*75*	*104*	*241*	
Pattern	*B*	*A*	*D*	*C*	*...*

K = 1.5 Sampling probability : B-66.7% A-33.3%

Fig. 1. A schematic illustration of the MPS-QS algorithm. The target image is shown in (a), with an unknown value *y* and its neighboring *N(y)* values (i.e., 10, 15, and 18). The training image is presented in (b), with an example of four patterns (A, B, C, and D). The patterns rank according to their distance from the neighboring *N(y),* and the sampling probability when *K* is equal to 1.5 is shown in (c).

illustrate the method. However, this search is not limited to a single image, and multiple training images can be used to find the best matching patterns to *N(y)*.

Two parameters in the MPS-QS algorithm require setting by calibration. The first is the neighborhood parameter *N* that determines the number of grid cells around *y* that make up the conditioning data *N(y)* in the target image. The second parameter is the sampling strategy parameter *K,* which Gravey and Mariethoz (2020) suggested setting to 1.2. The MPS-QS algorithm is described in detail by Gravey and Mariethoz (2020), and the readers can refer to their paper for further information.

3. Downscaling rainfall using the MPS model

In the previous section, we explained how the MPS-QS algorithm is used to complete missing data in target images using training images at the same resolution. In this section, we describe how the algorithm can be used to downscale rainfall.

3.1. Downscaling workflow

The model workflow is illustrated in Fig. 2, which shows a simple case of downscaling a single coarse-resolution image (Fig. 2a). Two datasets are required in the MPS downscaling approach: conditional and training images.

The conditional dataset comprises a conditional image (Fig. 2b) and a target image (Fig. 2e). The conditional image (Fig. 2b) is re-gridded from the coarse image (Fig. 2a) using a nearest-neighbor approach to the required downscaled resolution (i.e., the resolution of Fig. 2f). The target image has the same high grid resolution as that of the conditional image, and its values can be either empty or randomly sampled from the conditional image.

The training dataset comprises training images (Fig. 2d) and their corresponding upscaled training images (Fig. 2c). The training images have the same high resolution as the target image, and they can be either one or multiple images. The upscaled training images are obtained from upscaling the training images to the native resolution of the coarse image (i.e., that of Fig. 2a) by bicubic interpolation approach, then regridding the image using a nearest-neighbor method to match the same grid size to the target image. An iterative pattern search procedure (marked as 1 to 5 in Fig. 2) is taking place to define the rainfall intensities in the downscaled image (Fig. 2f): (1) for the unknown value *y* in the target image (Fig. 2e), a conditional pattern *N(y)* will be defined in the conditional image (Fig. 2b) at the location of *y*; (2) the MPS algorithm will match the most similar pattern in the upscaled-training image (Fig. 2c); (3) the location of the matched pattern is duplicated to the training image (Fig. 2d); (4) the corresponding rainfall value of the center of the matched pattern detected in the training image (Fig. 2d) is assigned to the unknown grid cell *y* in the target image (Fig. 2e) and downscaled image (Fig. 2f); and (5) this procedure continues until values are assigned to all the unknown grids in the downscaled image (Fig. 2f). It should be noted that due to the stochastic nature of the algorithm employed in the K-sampling strategy (Section 2 and Fig. 1c), downscaled images may differ slightly each time the algorithm is executed.

3.2. Inverting the areal reduction factor

When moving from a fine resolution to a coarse resolution, such as from a point scale (e.g. rain gauge) to an areal-averaged rainfall estimation (e.g. satellite), an areal reduction factor must be applied to account for the areal averaging of rainfall intensity (Sivapalan and Bloschl, 1998). With MPS-QS, the spatial structure of rainfall is preserved when rainfall fields are downscaled from coarse to fine resolution; but this is done without affecting rainfall intensities at the fine scale to reverse the effect of the areal reduction factor. In other words, the rainfall volumes

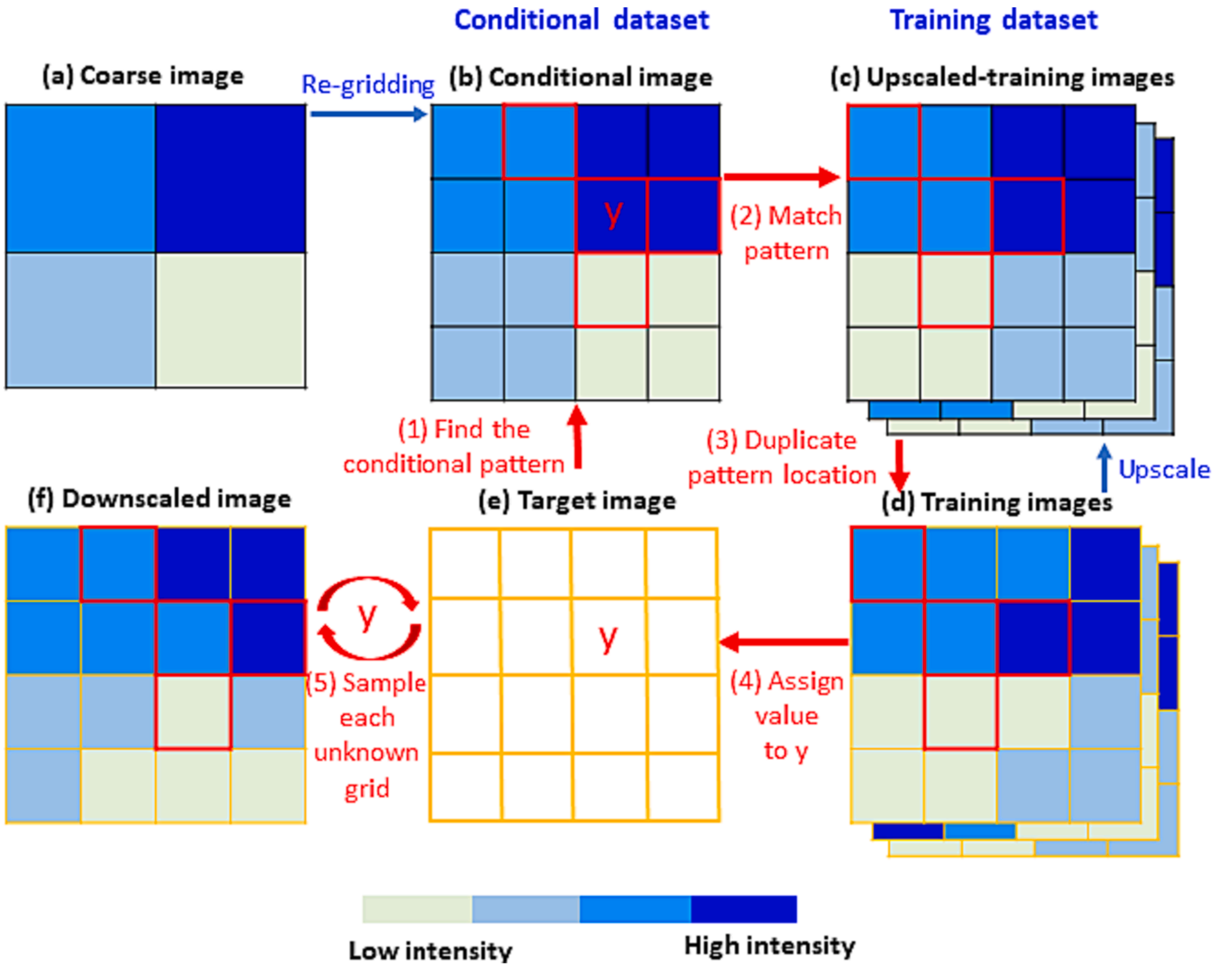

Fig. 2. An illustration of the MPS downscaling workflow (section 3.1 for details).

and averaged rainfall are preserved when downscaling with MPS-QS, but the rainfall extremes (both high and low intensities) are underestimated or overestimated as the rainfall variability is not increasing.

To simplify the problem of changes in rainfall intensities with spatial scales, we can consider the changes in rainfall spatial coefficient of variation (CV, defined as the ratio of the standard deviation to the mean of rainfall intensities per rainfall image). Moving toward finer spatial resolutions leads to an increase in rainfall spatial CV, a relationship that can be quantified using linear scaling laws (Peleg et al., 2018).

Therefore, we aim to adjust the CV of the downscaled rainfall by preserving the mean rainfall (μ) and changing the standard deviation (S). It can be written as:

$$\frac{S_D}{\mu} - \frac{S_D^*}{\mu} = CV_C - CV_D^* \tag{1}$$

where μ represents the mean rainfall intensities of the rainfall field, S_D represents the standard deviation of the downscaled rainfall computed from the MPS-QS output, S_D^* is the standard deviation of the adjusted downscaled rainfall after applying the CV adjustment, CV_C is the rainfall CV at the resolution of the coarse rainfall field (i.e., before downscaling), and CV_D^* is the adjusted CV at the downscaled resolution.

μ and S_D are known (can be computed directly from the downscaled image), and also CV_C and CV_D^* can be assumed to be known (based on scaling law analysis, e.g., Fig. S2). Hence, it seems there is a simple analytical solution (Eq. (1) to obtain S_D^* and adjust the downscaled rainfall image. But deriving S_D^* is likely to result in a considerable overestimation of the extreme rainfall in the downscaled image. Hence, we suggest finding S_D^* by optimization while constraining the upper rainfall percentile.

The optimization of S_D^* is done by minimizing Eq. (1), which is rewritten as:

$$S_D - S_D^* - (CV_C - CV_D^*)\mu \cong 0 \tag{2}$$

and it includes the constrain to the rainfall R at a specific quantile q (e.g., at the 99th percentile):

$$R_C(q) < R_D^*(q) < ZR_C(q) \tag{3}$$

where $R_C(q)$ and $R_D^*(q)$ indicate the extreme rainfall intensity at the coarse rainfall field and the adjusted downscaled rainfall field (respectively), and Z is a constant linear factor that can be derived from an estimate of an areal reduction factor (Le et al., 2018; Li et al., 2015; Pavlovic et al., 2016). Other optional constraints can be added to the optimization procedure; for example, as S_D^* can be computed analytically (from Eq. (1), one can constrain the optimized S_D^* value not to divert by more than a given percentiles from the expected S_D^* value.

Once S_D^* is found using Eq. (2) and the constrain of Eq. (3), we can adjust the rainfall quantiles q in the downscaled rainfall field R_D^* according to a distribution anamorphosis scheme (Peleg et al., 2017; Schleiss et al., 2012), which is defined as:

$$R_D^*(q) = F^{-1}[U(R_D(q))] \tag{4}$$

where U is the quantile function, and F^{1} is the inverse cumulative probability distribution function.

The proposed transformation of the rainfall intensities in the downscaled image can be easily implemented in most marginal distribution functions. As an example, we will use the Gamma distribution, one of the most widely used distributions to quantify rainfall intensity (Schleiss et al., 2012; Ulbrich, 1983; Yue et al., 2001), which is also the distribution we will use later in our case study. The Gamma distribution has two parameters: a shape parameter κ and a scale parameter θ. The mean and standard deviation are derived analytically as $\mu = \kappa\theta$ and $S = \sqrt{\kappa\theta^2}$, respectively. As such, Eq. (2) can be rewritten to explicitly find the k^* and θ^* parameters of the Gamma distribution function required for the transformation:

$$S_D - \sqrt{k^*\theta^{*2}} - (CV_C - CV_D^*)\mu \cong 0 \tag{5}$$

and Eq. (4) can then be rewritten for the explicit case of the Gamma distribution:

$$R_D^*(q) = G^{*-1}[G(R_D(q))] \tag{6}$$

where G is the quantile function of $Gamma(\kappa, \theta)$, which parameters are derived directly from the rainfall field R_D, and G^{*-1} is the inverse cumulative probability distribution function of $Gamma(k^*, \theta^*)$, which parameters are estimated by minimizing Eq. (5).

4. Case study

4.1. Beijing city

Beijing is located in the northern part of the North China Plain, bordered by the Yanshan Mountains in the north and the Taihang Mountains in the west. With over 21 million residents, Beijing is one of the largest cities in the world and is vulnerable to pluvial floods triggered by summer (convective) short-duration heavy rainfall (Fu et al., 2018; Hénonin et al., 2015; Yang et al., 2017). Elevation increases from southeast to northwest in the region, while rainfall decreases (Fig. 3). The climate in the Beijing area is classified as a monsoon-influenced humid continental climate, which is characterized by hot and humid summers and cold and dry winters. The annual average rainfall is around 600 mm, with 72.5 % of precipitation occurring during the summer months of June, July, and August (Yin et al., 2011; Zhai et al., 2014; Zou et al., 2021).

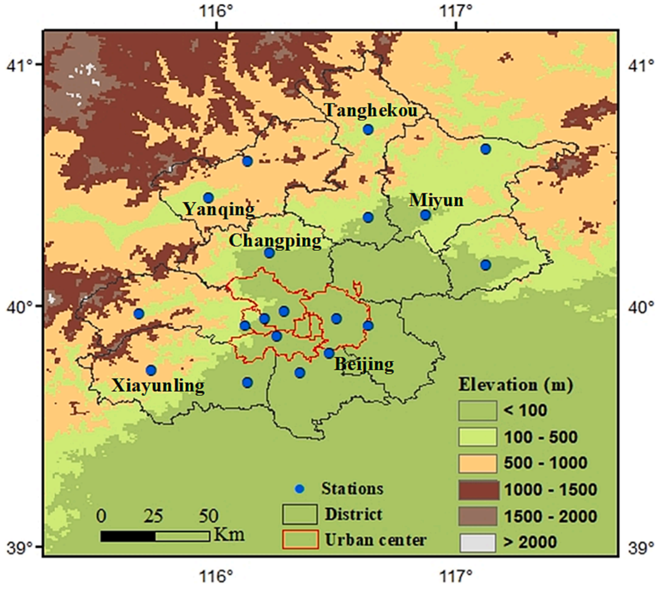

Fig. 3. A map of the study area.

4.2. Data

The coarse rainfall fields (target images) to be downscaled are the bias-corrected version of the Climate Prediction Center Morphing (CMORPH, Xie et al., 2017), which covers the period from 1998 to 2019 with temporal and spatial resolutions of 30 min and 8 km, respectively. The high spatial–temporal resolution of the rainfall data is suitable for urban hydrological applications (Ochoa-Rodriguez et al., 2015), and the length of the data meets the requirements for analyzing rainfall extremes (Marra et al., 2017). CMORPH has been used to analyze extreme rainfall in China's major metropolitan areas (Chen et al., 2015; Fu et al., 2019; Wang et al., 2021; Xing et al., 2019) in the past.

As training images, high spatial resolution rainfall fields from the China Meteorological Administration (CMA) Multisource-merged Precipitation Analysis System product (CMPAS, Shen et al., 2018) are used. CMPAS has a resolution of 1 h and 1 km, which is obtained by merging with weather radar, ground station, and CMORPH data within China. This product is relatively new and spans six years from 2015. It would be an ideal dataset for analyzing extreme rainfall impacts on floods in urban regions, but its short period prevents direct use in this context. However, its high spatial resolution and quality make it a great candidate for image training. The purpose of this case study is to demonstrate spatial downscaling of rainfall using the MPS-QS algorithm without taking into consideration the temporal differences between rainfall products. For this reason, we aggregated the CMORPH data from 30 min to 1 h to match the CMPAS data.

To assist in validating the MPS-QS downscaling results, we also extracted hourly rainfall data from nineteen climate stations (see their locations in Fig. 3), operated by China Meteorological Administration (CMA). Their data include 58 years between 1954 and 2012.

4.3. Model parameters

As described in Sections 2 and 3, the MPS-QS includes a few parameters that need to be calibrated or set. Based on trial and error (not shown), we found setting the parameters $N(y)$ to 15 and K to 1.2 ideal for our downscaling purposes.

The CV scaling required to adjust the downscaled rainfall image was computed by upscaling the CMPAS product from 1 km to 20 km resolution (Fig. S2). The specific quantile q to constrain the rainfall adjustment was set to 0.99; this is an arbitrary but common choice, as rainfall extreme is often referred to as the 99th percentile. Based on the literature (e.g., Li et al., 2015; Pavlovic et al., 2016), we set Z, representing the rainfall difference at the 99th quantile between 8 km and 1 km, to 10. The Nelder-Mead simplex algorithm (Lagarias et al., 1998) search method was used for the minimum optimization of Eq. (5).

4.4. Model evaluation criteria

A simple bias skill was used to evaluate the results of the MPS-QS downscaling on rainfall intensities, i.e., the difference in percentages or the ratio between the downscaled and observed or expected rainfall values. The rainfall spatial structures were evaluated using a variogram (Armstrong, 1998; Benoit and Mariethoz, 2017):

$$\gamma(h) = \frac{1}{2n(h)} \sum_{i=1}^{n(h)} (R(i) - R(i+h))^2 \tag{7}$$

where $R(i)$ and $R(i+h)$ are rainfall intensities at grid cell i and grid cell $i+h$ at the same rainfall field (image), with h being the distance between them, and $n(h)$ is the number of the pairs of rainfall intensities separated by distance h. The value where the variogram stabilized is called sill, which describes the average variance of the rainfall over the domain; and the distance where the sill value is reached is called range, which represents the smallest decorrelation distance or the size of rainfall spatial patterns.

4.5. *Example: Downscaling of a single rainfall field*

An extreme hourly rainfall event that occurred on the 20th of July 2016 was selected as an example to demonstrate the downscaling process and efficacy of the method. Based on the CMPAS data, we obtained the rainfall field recorded at 10 am (Fig. 4a) and upscaled it from 1 km to 8 km resolution (Fig. 4b) by simple averaging. We treated the original rainfall field at 1 km resolution as our "ground truth" (i.e., the image we intended at the end of the downscaling procedure). In this way, our desired high-resolution rainfall field is not hidden and can be compared to the downscaled rainfall field. The next step was to run the MPS-QS algorithm and downscale the rainfall field to its native resolution of 1 km (Fig. 4c). All the CMPAS data, excluding this particular hourly rainfall field, were used as training images. The best three training images matching the hourly rainfall were ultimately used by the algorithm. Finally, we inverted the areal reduction factor using the CV adjustment method and obtained an adjusted downscaled image (Fig. 4d).

Several properties of the rainfall field can now be compared, beginning with the mean areal rainfall (MAR). MAR difference between the coarse-scale rainfall field (Fig. 4b) and downscaled rainfall field (Fig. 4c) is as low as 1.2 %, implying that rainfall mass is preserved during downscaling. But both rainfall CV and extreme rainfall intensity (equivalent to the 99th percentile in this case) decrease with downscaling by 7 % and 8 % (respectively, Fig. 4b-c). However, because of adjusting the downscaled rainfall field using the scaled CV, we can obtain an adjusted downscaled image (Fig. 4d) with MAR, CV, and extreme rainfall intensity values similar to those found in the ground truth (Fig. 4a), resulting in biases of less than 2 % for all factors (Fig. 4e). To estimate the spatial structure of the adjusted downscaled rainfall field (Fig. 4d) with the ground truth image (Fig. 4a), we plotted their variograms in Fig. 4f. At a distance of approximately 60 km, both variograms show the same decorrelation range. The bias in the average variance (sill) between variograms is around 12 %, which can be partially attributed to the fact that the original rainfall field (Fig. 4a) is affected by radar artifacts (for example, beam blockage; note the arcs and straight lines in the figure without any data) that are removed by the MPS algorithm (Fig. 4d). Based on this, we conclude that the spatial rainfall structure has been preserved in downscaling, as can also be visually seen when comparing Fig. 4a and d.

4.6. *An evaluation of the downscaling method*

The downscaling method was evaluated using a similar approach to that presented in the previous section. From the 1 km CMPAS data, 10 heavy summer (convective) rainfall events with more than 200 rainfall fields were selected. The fields were upscaled to 8 km by averaging and then downscaled again to 1 km resolution by applying the MPS-QS method using the leave-one-out cross-validation approach (i.e., downscaled rainfall fields were not included in the training data). Then the downscaled rainfall fields were adjusted by inverting the areal reduction factor. Rainfall intensities and structures were compared between the original 1 km images and the adjusted downscaled images.

In terms of rainfall intensities, the MPS-based downscaling with the CV adjustment method effectively preserved MAR, as demonstrated by a low bias of 2 % (Fig. 5a). Similarly, CV is well conserved (with *a* bias of 2 %) in downscaled rainfall fields, although it tends to be slightly underestimated when CV exceeds 8 on rare occasions (Fig. 5b). Furthermore, the downscaling method reproduces extreme rainfall intensities at the 99th percentile with an average overestimation of only 6 % (Fig. 5c).

Variograms were compared to assess the rainfall spatial structure. The average bias between the variograms at distances of 20 km, which is

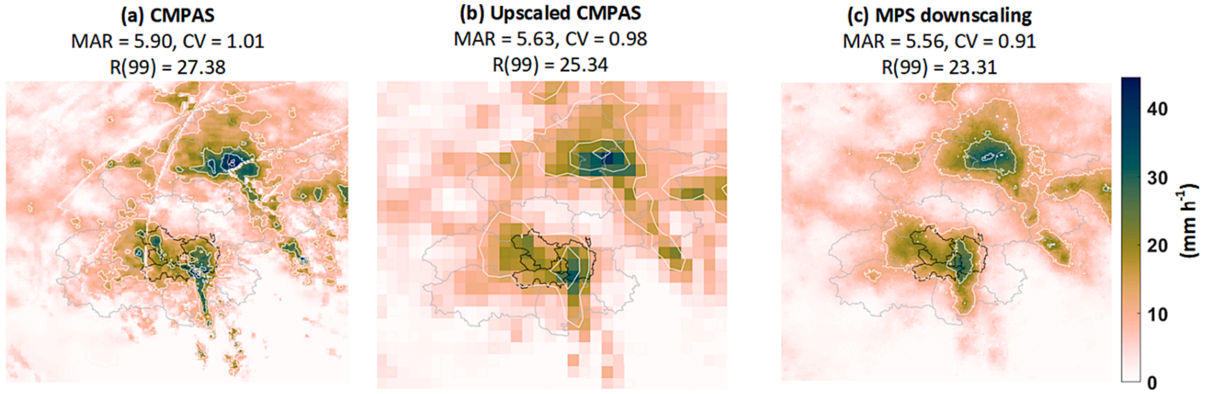

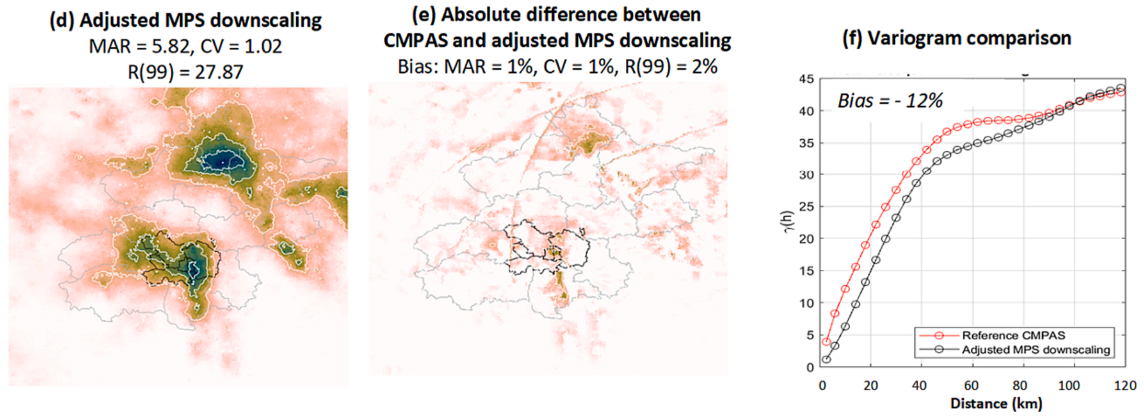

Fig. 4. Downscaling the hourly rainfall field recorded by CMPAS (a) at 10 am, on the 20th of July 2016. The rainfall field was upscaled to 8 km (b), downscaled by the MPS-QS (c), and adjusted for the rainfall CV (d). (e) and (f) present the absolute difference between the original and downscaled images (i.e., |d-a|) and their variograms (respectively).

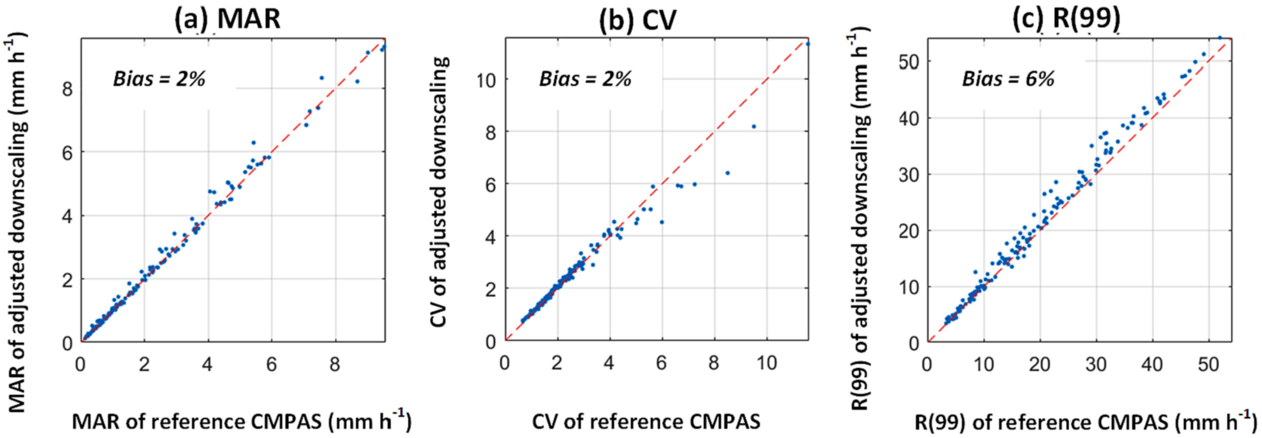

Fig. 5. Comparison of mean areal rainfall (a), rainfall spatial CV (b), and extreme rainfall intensity at the 99th percentile (c) between reference CMPAS rainfall fields and downscaled rainfall fields using the MPS-QS method.

well within the range of rainfall correlation in this region (see for example Fig. 4f), amounts to only 4 %. By examining the bias at distances of 80 km, often where the rainfall fields are no longer spatially correlated, the bias increases to 12 %. In light of these results, it appears that the downscaling method is capable of reproducing realistically the spatial structure of rainfall. Nevertheless, we also evaluated the method's ability to reproduce rainfall structures for different rainfall types while downscaling. We focused on four common rainfall cases: stratiform homogeneously-distributed rainfall (Fig. 6a), a scattering of convective cells (Fig. 6b), a convective squall line (Fig. 6c), and a clustered convective cell (Fig. 6d).

When comparing the reference CMPAS and adjusted downscaled rainfall images, the stratiform homogeneously-distributed storm shows comparable rainfall fields and variogram patterns (Fig. 6a). The variograms agree up to a distance of 20 km, then diverge, resulting in a 12 % bias. Nevertheless, decorrelation distances for both images are similar at approximately 80 km. A similar pattern was found when downscaling the rainfall field characterized by scattered convective cells (Fig. 6b). Variograms, in this case, are also similar up to the 20 km distance, but since the rainfall intensity is stronger (up to 100 mm h^{-1}), a higher bias (19 %) is found. When a convective square line (Fig. 6c) and a clustered convective cell (Fig. 6d) are downscaled, variogram similarity levels are even more prominent, with decorrelation distances around 60 km and bias levels as low as 4 %. Considering that most of the bias is derived above the rainfall decorrelation distances and that the shape of the variograms is essentially the same, we conclude that the spatial structure of the rainfall fields is satisfactorily reproduced.

Accordingly, the results presented above demonstrate that MPS-based downscaled images with the suggested adjustment are capable of reproducing both rainfall intensity (Fig. 5) and the spatial structure of rainfall fields (Fig. 6) of various rainfall types.

5. Downscaling 22 years of CMORPH data

Using the MPS-QS model and the adjusted algorithm discussed above, 22 years of CMORPH data were downscaled from 8 km to 1 km resolution in the Beijing area. As our focus is on heavy convective rainfall events, the results for the downscaled summer rainfall are presented here, while the autumn and spring rainfall are shown in Fig. S3 and S4 (respectively).

We start by exemplifying downscaling of a single heavy rainfall, an hourly 8-km coarse-resolution CMORPH rainfall image from the 21st of July 2012 (Fig. 7a). Two downscaled images from the MPS-QS model before and after applying the CV adjustment are presented in Fig. 7c and e, and are zoomed-in in Fig. 7d and f, respectively. The MAR is well preserved comparing the coarse resolution image (11.3 mm h^{-1}) and the downscaled images (11.4 and 11.8 mm h^{-1}), with a difference of only 4 % between the images. As expected, the CV is identical in the coarse image and downscaled image (1.08 and 1.07), and increased following the adjustment to 1.1. Similarly, the intense rainfall at the 99th percentile is the same, comparing the coarse and downscaled images (56.1 and 56.3 mm h^{-1}), and increased following the adjustment to 61.7 mm h^{-1}; an increase of 10 % that is following the 10 % intensification expected when applying the inverse areal reduction factor between 8 km and 1 km scales (see discussion above).

Next, we summarize the statistics of all the downscaled CMORPH hourly summer rainfall fields. The adjusted MPS downscaled images maintain adequate MAR values with an average overestimation bias of 3 % (Fig. 8a). In general, CV values are increasing (average positive bias of 4 %); however, there are some images in which CV values are decreasing (Fig. 8b). Furthermore, all downscaled images show an increase in heavy rainfall intensity (at the 99th percentile Fig. 8c). Following the adjustment algorithm, extreme rainfall intensity increases by 8 % on average, which is not far from the expected 10 % intensification when moving from 8 km to 1 km resolution.

We also examined the ability of downscaled rainfall to spatially reproduce extreme rainfall intensities. To this end, we calculated the annual maximum rainfall from the adjusted MPS downscaled images and used the Weibull distribution to calculate the extreme rainfall at the 2, 5, 10, and 30-year return levels. This procedure was repeated with the hourly rainfall data collected from 19 ground stations within the Beijing area (Fig. 3). For all return periods, the most severe rainfall intensities were detected over or around 20 km northeast of Beijing station (Fig. 9). The return levels of downscaled CMORPH correspond well to at least half of the stations (10 out of 19) within this study area, including the Beijing station that represents the rainfall over the urban area. The underestimation between the downscaled and the observed extremes are on average 10 mm h^{-1} for the 2- to 10-year return level and around 20 mm h^{-1} for the 30-year return level. This underestimation is attributed to the different periods used for the estimation of the rainfall extremes between the downscaled CMORPH (1998–2019) and the stations (1998–2012), and due to the difference in spatial scales, i.e., between 1 km (downscaled product) and point scale (ground stations).

The final example will demonstrate the MPS model's ability to downscale a rainfall event over several hours while maintaining realistic rainfall patterns in space and time (Fig. 10). We have chosen six images (hours) of a storm that crossed Beijing between 10 am and 3 pm on 21st of July 2012. It was one of the most extreme storms that hit the city, with hourly rainfall ranging between 36.7 and 63.6 mm h^{-1}. The downscaled rainfall fields largely maintain the spatial structure and volume of the coarse images, but increase the CV and maximum rainfall intensity, as expected (refer to the labels located above the images in Fig. 10).

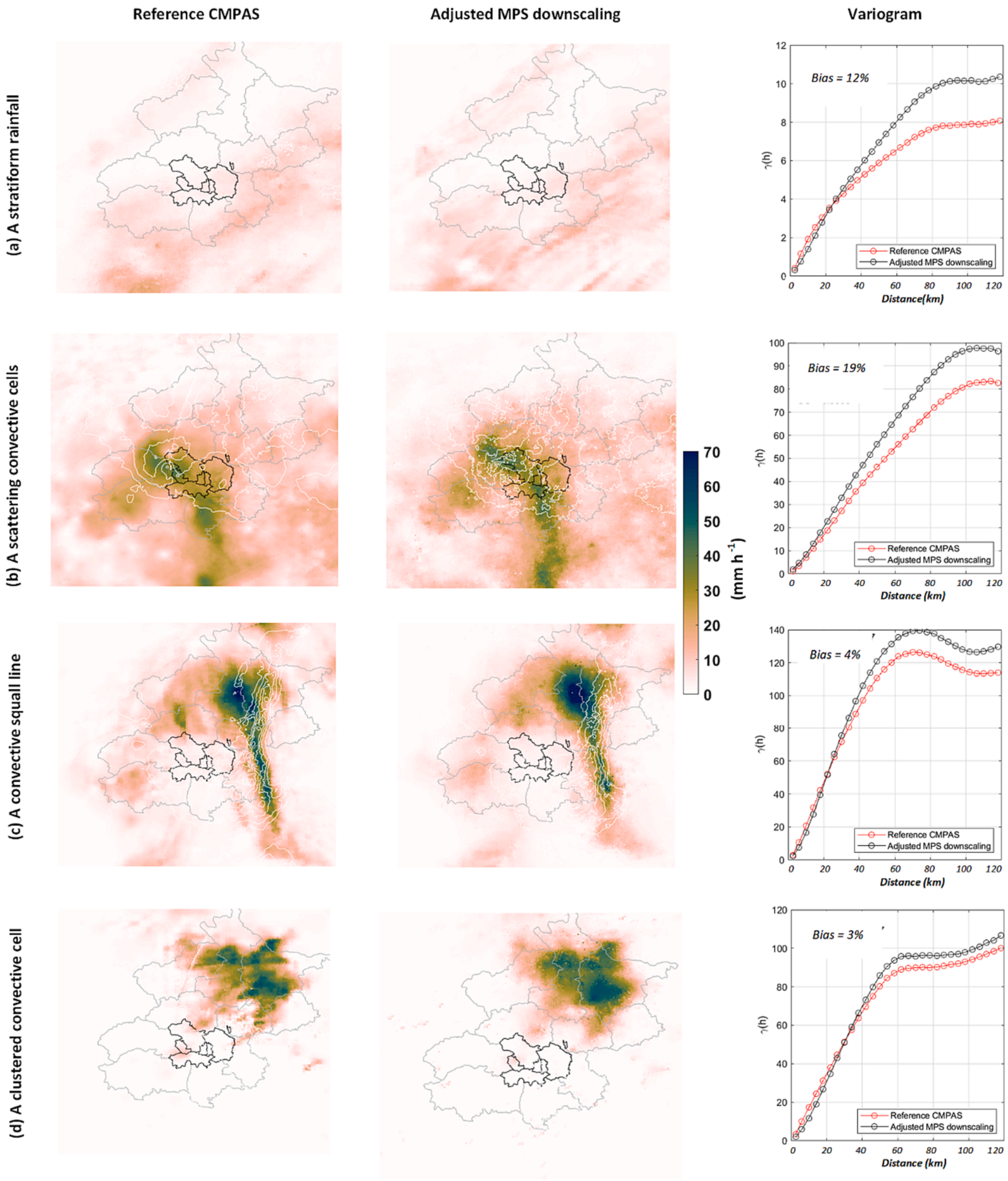

Fig. 6. Reference (left, CMPAS images at 1 km) and downscaled (center, MPS-QS adjusted images at 1 km) four common rainfall types: (a) a stratiform rainfall, (b) a scattering of convective cells, (c) a convective squall line, and (d) a clustered convective cell, and their variograms (right).

Despite the absence of a temporal autocorrelation function in MPS-QS, it appears that the rainfall fields are adequately downscaled not only spatially but over time as well.

6. Discussion

6.1. MPS-QS model parameters

We set $N(y)$, which defines the number of grid cells to be used when searching for the most suitable pattern match in the training images, to

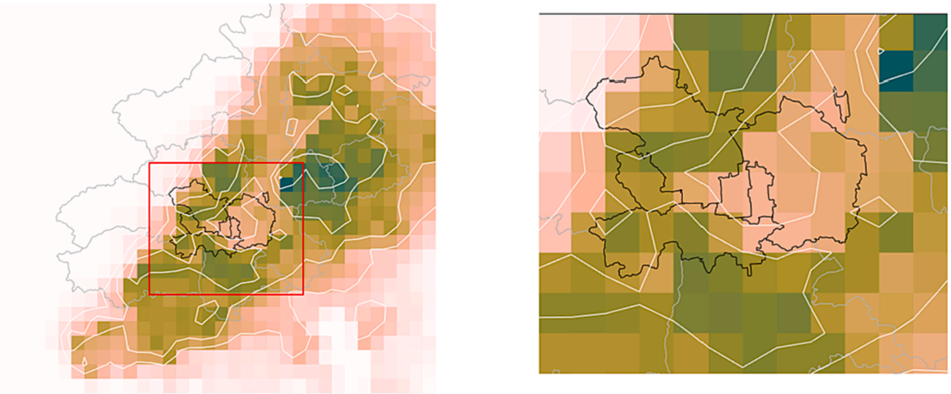

(a) CMORPH
MAR = 11.28, CV=1.08
R(99) = 56.11

(b) CMORPH
zoom in

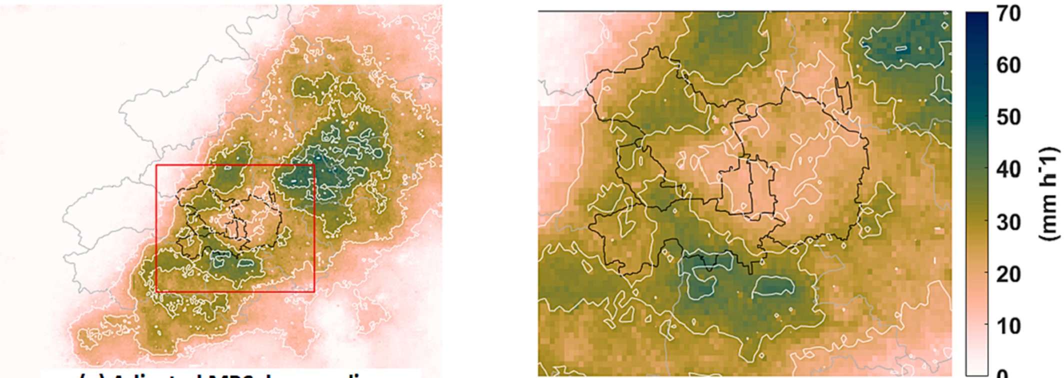

(c) MPS downscaling
MAR = 11.41, CV=1.07
R(99) = 56.35

(d) MPS downscaling
zoom in

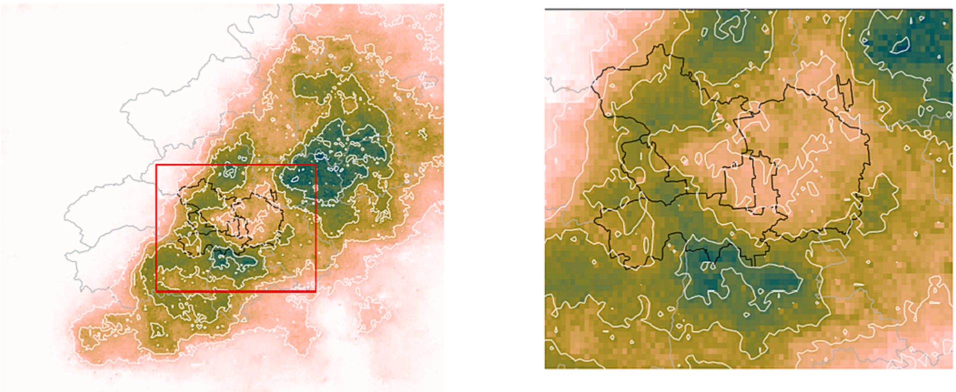

(e) Adjusted MPS downscaling
MAR = 11.79, CV=1.10
R(99) = 61.72

(f) Adjusted MPS downscaling
zoom in

Fig. 7. The hourly rainfall field derived from the CMORPH data (8 km) on the noon of the 21st of July 2012 (a, b), the MPS downscaling images at 1 km (c, d), and the rainfall images at 1 km after applying the adjustment algorithm (e, f).

15; within the suggested range of 15 to 25 (Gravey and Mariethoz, 2022; 2020). In their application to the MPS model with a similar domain size, Singhal and Jha (2022) used a similar value ($N(y)$ equals 14). While it seems possible to fix $N(y)$ value to this range, Gravey and Mariethoz (2022) mentioned that the optimal parameter value can also depend on the training dataset, thus calibration is recommended. This can be accomplished by upscaling several images from the training data and downscaling them again to their native resolution, as described in Section 4.5, while varying $N(y)$. The same applies to the K parameter. In our case study, it was set to 1.2, as recommended by Gravey and Mariethoz (2020; 2022), and the authors suggest the use of $k > 1$, to reduce the issue of a verbatim copy of the training image. Since MPS-QS has only two parameters to consider, and both of them can be easily adjusted to optimize the model's performance, the model is both simple and flexible, making it appealing to end users.

6.2. *Training data*

The training data we used for this study consisted of 6 years' worth of hourly CMPAS rainfall fields, which amounted to more than 52,000 images in total. Since the model was based upon a seasonal framework (hence a quarter of the images were used per season), and since many of

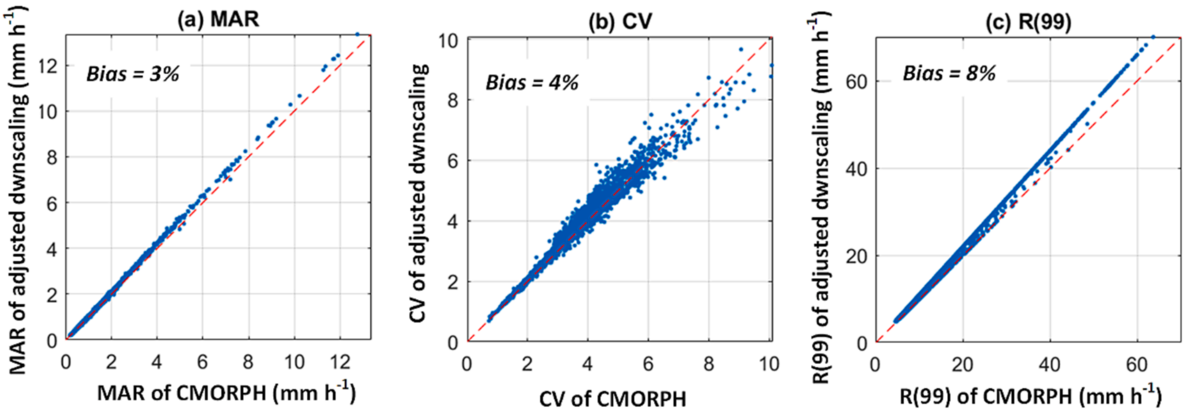

Fig. 8. Comparing MAR (a), CV (b), and the heaviest 99th percentile rainfall intensity (c) between 8-km CMORPH and 1-km adjusted MPS downscaling.

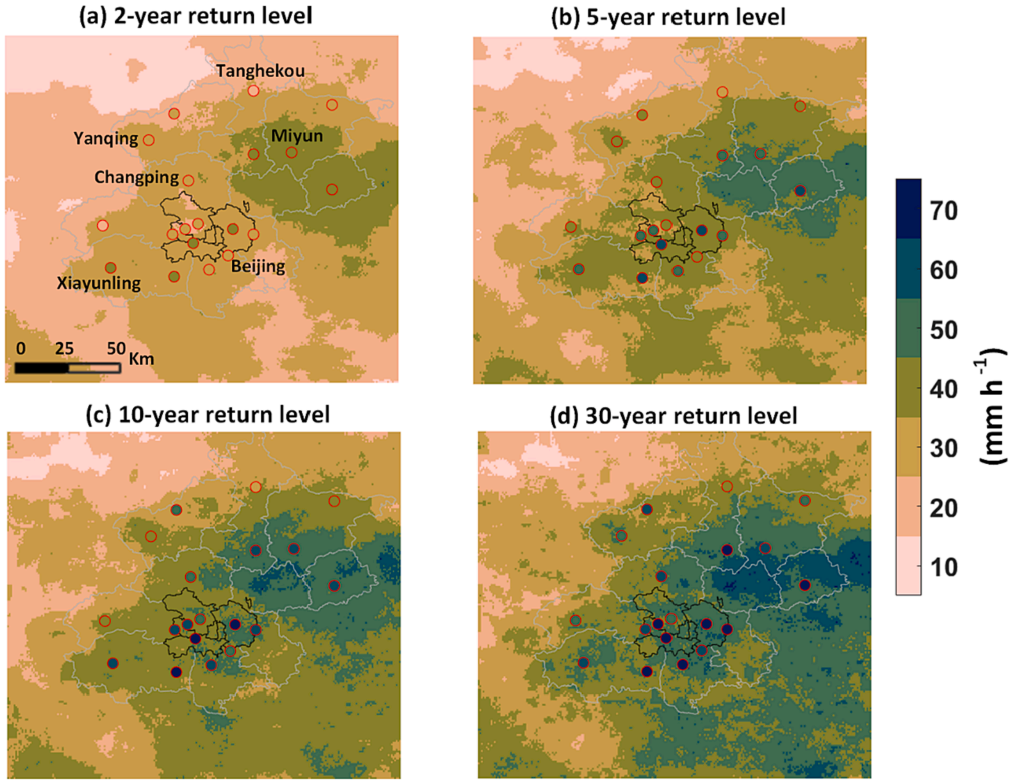

Fig. 9. Comparison of (a) 2, (b) 5, (c) 10, and (d) 30-year return levels between the adjusted MPS downscaling and nineteen stations (red circles). (For interpretation of the references to colour in this figure legend, the reader is referred to the web version of this article.)

the hourly images occur during periods of rainfall intermittency (i.e., when no rainfall is recorded), there is a substantial reduction in the number of images that are effectively available. Nevertheless, there were still approximately 6500 training images with the potential to be used; according to our downscaling results (e.g., Figs. 8 and 9), this appears to be an adequate number of images for model training. For a comparison, Jha et al. (2015) had around 7300 training images to downscaled one-year daily precipitation from 50 km to 10 km, and Singhal and Jha (2022) had around 1500 training images to downscale daily precipitation for the monsoon season from 30 km to 10 km. Their conclusion was similar to ours in that this number of images was adequate to meet their needs. Furthermore, an average of three best training images for each downscaled hourly CMORPH rainfall are used in the study. When enough data are available, increasing numbers of training images contribute to enhanced downscaling accuracy. However, this improvement is accompanied by a proportional increase in computational time. The determination of the optimal number of training images can not be defined a priori, as it depends on the user's available data and computational resources.

Nevertheless, it is apparent that the broader the number of rainfall images available for the model training, the better the downscaling results may be. Training images do not need to come from the same domain as the domain of interest. Yin et al. (2022), for example, used the MPS with training images from the Artic area to improve digital elevation resolution in Antarctica. Therefore, as long as the rainfall space–time patterns are the same, it is possible to extend the training images for rainfall downscaling by taking high-resolution images from a different location. The number of training images can also be increased by using images obtained from multiple other sources. For example, Singhal and Jha (2022) not only used precipitation data but also used temperature, latitude, longitude, and elevation variates as training images to downscale daily precipitation in the northwest Himalayas area.

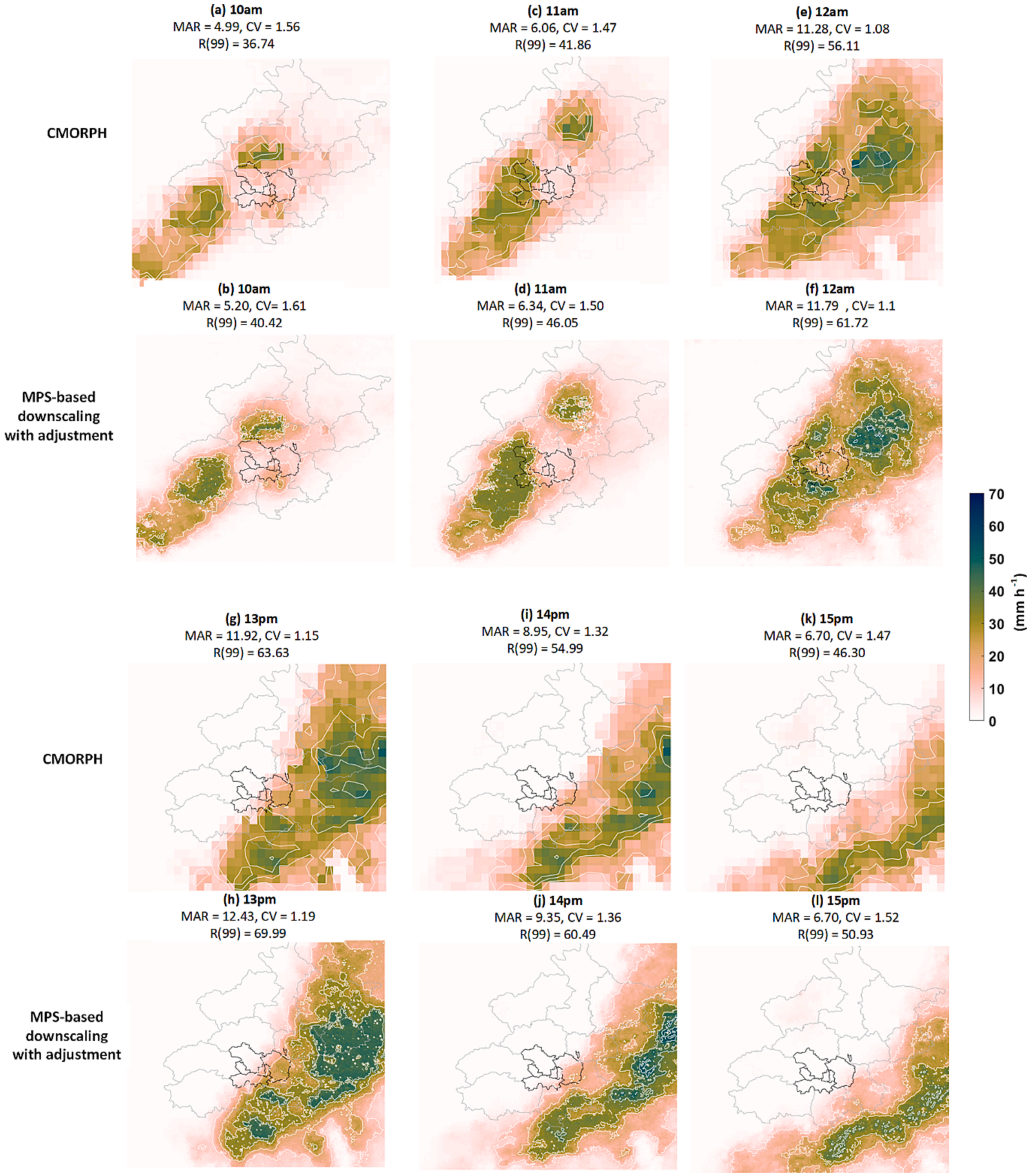

Fig. 10. An example of a downscaled storm from 10 am to 3 pm on the 21st of July 2012. (a), (c), (e), (g), (i), and (k) are the hourly 8-km CMORPH rainfall images, and below them are the corresponding 1-km adjusted downscaled MPS-QS images [(b), (d), (f), (h), (j), and (l)].

Since complex terrain (Roe, 2005) and large metropolitan areas (Yang et al., 2014; Zhang, 2020) can affect rainfall space–time patterns, it is important to consider this when selecting the domain and source of the training images.

6.3. The areal adjustment method

The proposed areal reduction adjustment requires input from users on two aspects: how the areal reduction factor affects extreme rainfall when moving between scales, as well as which marginal distribution method best characterizes the spatial distribution of rainfall intensity. The 99th rainfall percentile was defined in our case study as the anchor for adjusting extreme rainfall following the areal reduction factor. However, this is an arbitrary definition that can be modified by the users, as extreme rainfall intensity can be defined by a wide range of percentiles, from 95th to 99.9th (Fischer and Knutti, 2016; Zhang et al., 2017). Furthermore, in our application, we considered a reduction factor value obtained from the literature (Pavlovic et al., 2016), but users may choose to upscale the training images to the scale of the coarse images and compute the reduction factor directly (for example, as Peleg et al., 2018 did).

It is possible to evaluate the rainfall adjustment procedure by comparing the adjusted rainfall CV values to their theoretical values after downscaling (e.g., Fig. S2). Biases from the theoretical values are in the range of 20 %, varying from −60 % to 10 % based on the adjusted rainfall CV (Fig. 11). As we are interested in downscaling heavy rainfall in our area, and as it is primarily spatially heterogeneous summer convection (CV greater than 4), we conclude that we are generally within 10 % agreement with the theoretically expected CV values. However, this is only a first-order evaluation based on theoretical values, as we lack ground truth.

To describe rainfall intensity in space, we found that the Gamma distribution is most appropriate for fitting to summer heavy rainfall in Beijing. The Gamma distribution is widely used to capture rainfall intensity worldwide (Yue et al., 2001). Different marginal distributions can, however, be tested and applied as they may be more appropriate in different regions and climates characterized by different rainfall types.

7. Conclusions

Further development of the MPS-QS model is presented and demonstrated to downscale satellite-derived gridded rainfall series based on a few years of high-resolution rainfall observations. The method is light in terms of parameterization, requiring only decisions from the end-user on the model's sampling strategy (two parameters), how extreme rainfall intensities and rainfall spatial heterogeneity are scaled, and the marginal distribution that best describes how rainfall is distributed in space. This required information can be obtained directly from the training data (i.e., the high-resolution rainfall fields) provided as input to the model. By using rainfall data from the Beijing area as a case study, we demonstrate that the downscaling method can both accurately represent rainfall intensities while preserving rainfall spatial structure, and even correct rainfall images if rainfall intensities are partially missing. We focused primarily on downscaling heavy summer rainfall, but the method can be applied to other types of rainfall and to other climates as long as sufficient high-resolution rainfall data are available to train the model.

Code and data availability

The MPS-QS algorithm can be accessed from the GAIA website (https://github.com/GAIA-UNIL/G2S). And an example of the MPS-based downscaling method can be found in the Zenodo archive at https://zenodo.org/records/10497207. This code example reproduces Fig. 4 from the manuscript. The CMPAS data can be accessed from the China Meteorological Administration (Shen et al., 2018).

CRediT authorship contribution statement

Wenyue Zou: Formal analysis, Methodology, Software, Writing – original draft, Writing – review & editing. **Guanghui Hu:** Software. **Pau Wiersma:** Software, Writing – review & editing. **Shuiqing Yin:** Writing – review & editing. **Yuanyuan Xiao:** Visualization. **Grégoire Mariethoz:** Conceptualization, Methodology, Software, Writing – review & editing. **Nadav Peleg:** Conceptualization, Methodology, Writing – review & editing.

Declaration of competing interest

The authors declare that they have no known competing financial interests or personal relationships that could have appeared to influence the work reported in this paper.

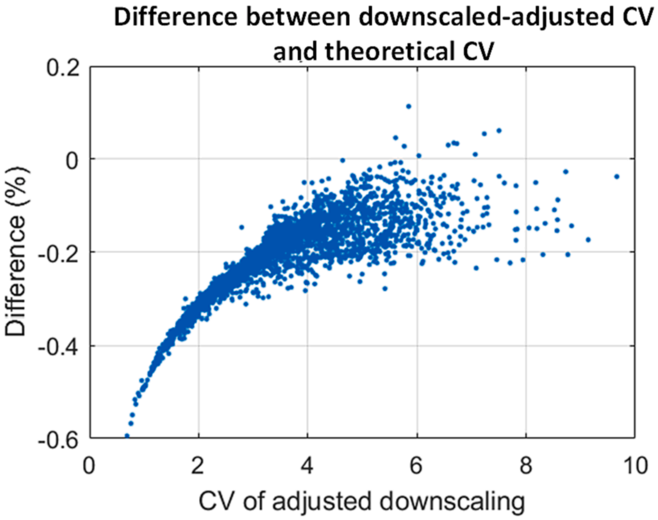

Fig. 11. The difference between the downscaled-adjusted CV and its theoretical values.

Data availability

Data will be made available on request.

Acknowledgements

WZ acknowledges the support of the China Scholarship Council (CSC. Grant number: 202106040028) and NP acknowledges the support of the Switzerland Nation Science Foundation (SNSF. Grant number: 194649, Rainfall and floods in future cities).

Appendix A. Supplementary data

Supplementary data to this article can be found online at https://doi.org/10.1016/j.jhydrol.2024.130899.

References

Abdollahipour, A., Ahmadi, H., Aminnejad, B., 2022. A review of downscaling methods of satellite-based precipitation estimates. Earth Sci. Inform. 15, 1–20. https://doi.org/10.1007/s12145-021-00669-4.

Armstrong, M., 1998. The Variogram, in: Armstrong, M. (Ed.), Basic Linear Geostatistics. Springer, Berlin, Heidelberg, pp. 25–46. https://doi.org/10.1007/978-3-642-58727-6_3.

Benoit, L., Mariethoz, G., 2017. Generating synthetic rainfall with geostatistical simulations. Wires Water 4, e1199.

Chen, C., Hu, B., Li, Y., 2021. Easy-to-use spatial random-forest-based downscaling-calibration method for producing precipitation data with high resolution and high accuracy. Hydrol. Earth Syst. Sci. 25, 5667–5682. https://doi.org/10.5194/hess-25-5667-2021.

Chen, S., Li, W.-B., Du, Y.-D., Mao, C.-Y., Zhang, L., 2015. Urbanization effect on precipitation over the Pearl River Delta based on CMORPH data. Adv. Clim. Change Res. 6, 16–22. https://doi.org/10.1016/j.accre.2015.08.002.

Chen, Q., Mariethoz, G., Liu, G., Comunian, A., Ma, X., 2018. Locality-based 3-D multiple-point statistics reconstruction using 2-D geological cross sections. Hydrol. Earth Syst. Sci. 22, 6547–6566. https://doi.org/10.5194/hess-22-6547-2018.

Cristiano, E., ten Veldhuis, M., van de Giesen, N., 2017. Spatial and temporal variability of rainfall and their effects on hydrological response in urban areas - a review. Hydrol. Earth Syst. Sci. 21, 3859–3878. https://doi.org/10.5194/hess-21-3859-2017.

Cui, Z., Chen, Q., Liu, G., Mariethoz, G., Ma, X., 2021. Hybrid parallel framework for multiple-point geostatistics on Tianhe-2: A robust solution for large-scale simulation. Comput. Geosci. 157, 104923 https://doi.org/10.1016/j.cageo.2021.104923.

Dao, D.A., Kim, D., Kim, S., Park, J., 2020. Determination of flood-inducing rainfall and runoff for highly urbanized area based on high-resolution radar-gauge composite rainfall data and flooded area GIS data. J. Hydrol. 584, 124704 https://doi.org/10.1016/j.jhydrol.2020.124704.

Fischer, E.M., Knutti, R., 2016. Observed heavy precipitation increase confirms theory and early models. Nat. Clim. Change 6, 986–991. https://doi.org/10.1038/nclimate3110.

Fu, C., Liu, J., Wang, H., Xiang, C., Fu, X., Luan, Q., 2018. Urban storm flooding: Characteristics and management in Beijing. MATEC Web Conf. 246, 01042. https://doi.org/10.1051/matecconf/201824601042.

Fu, X., Yang, X.-Q., Sun, X., 2019. Spatial and Diurnal variations of summer hourly rainfall over three super city clusters in eastern China and their possible link to the urbanization. J. Geophys. Res. Atmos. 124, 5445–5462. https://doi.org/10.1029/2019JD030474.

Gravey, M., Mariethoz, G., 2020. QuickSampling v1.0: A robust and simplified pixel-based multiple-point simulation approach. Geosci. Model Dev. 13, 2611–2630. https://doi.org/10.5194/gmd-13-2611-2020.

Gravey, M., Mariethoz, G., 2022. AutoQS v1: Automatic parameterization of QuickSampling based on training images analysis. Geosci. Model Dev. Discuss. 1–21 https://doi.org/10.5194/gmd-2022-229.

Gribov, A., Krivoruchko, K., 2020. Empirical Bayesian kriging implementation and usage. Sci. Total Environ. 722, 137290 https://doi.org/10.1016/j.scitotenv.2020.137290.

Guardiano, F.B., Srivastava, R.M., 1993. Multivariate Geostatistics: Beyond Bivariate Moments, in: Soares, A. (Ed.), Geostatistics Tróia ʾ92: Volume 1, Quantitative Geology and Geostatistics. Springer Netherlands, Dordrecht, pp. 133–144. https://doi.org/10.1007/978-94-011-1739-5_12.

Hénonin, J., Hongtao, M., Zheng-Yu, Y., Hartnack, J., Havnø, K., Gourbesville, P., Mark, O., 2015. Citywide multi-grid urban flood modelling: the July 2012 flood in Beijing. Urban Water J. 12, 52–66. https://doi.org/10.1080/1573062X.2013.851710.

Huuskonen, A., Saltikoff, E., Holleman, I., 2014. The operational weather radar network in Europe. Bull. Am. Meteorol. Soc. 95, 897–907. https://doi.org/10.1175/BAMS-D-12-00216.1.

Jha, S.K., Mariethoz, G., Evans, J., McCabe, M.F., Sharma, A., 2015. A space and time scale-dependent nonlinear geostatistical approach for downscaling daily precipitation and temperature. Water Resour. Res. 51, 6244–6261. https://doi.org/10.1002/2014WR016729.

Joyce, R.J., Janowiak, J.E., Arkin, P.A., Xie, P., 2004. CMORPH: A Method that produces global precipitation estimates from passive microwave and infrared data at high spatial and temporal resolution. J. Hydrometeorol. 5, 487–503. https://doi.org/10.1175/1525-7541(2004)005<0487:CAMTPG>2.0.CO;2.

Karger, D.N., Conrad, O., Böhner, J., Kawohl, T., Kreft, H., Soria-Auza, R.W., Zimmermann, N.E., Linder, H.P., Kessler, M., 2017. Climatologies at high resolution for the earth's land surface areas. Sci. Data 4, 170122. https://doi.org/10.1038/sdata.2017.122.

Lagarias, J.C., Reeds, J.A., Wright, M.H., Wright, P.E., 1998. Convergence properties of the Nelder-mead simplex method in low dimensions. SIAM J. Optim. 9, 112–147. https://doi.org/10.1137/S1052623496303470.

Le, P.D., Davison, A.C., Engelke, S., Leonard, M., Westra, S., 2018. Dependence properties of spatial rainfall extremes and areal reduction factors. J. Hydrol. 565, 711–719. https://doi.org/10.1016/j.jhydrol.2018.08.061.

Li, J., Sharma, A., Johnson, F., Evans, J., 2015. Evaluating the effect of climate change on areal reduction factors using regional climate model projections. J. Hydrol. 528, 419–434. https://doi.org/10.1016/j.jhydrol.2015.06.067.

MacKie, E.J., Schroeder, D.M., Caers, J., Siegfried, M.R., Scheidt, C., 2020. Antarctic Topographic realizations and geostatistical modeling used to map subglacial lakes. J. Geophys. Res.-Earth Surf. 125 https://doi.org/10.1029/2019JF005420.

Mariethoz, G., Caers, J., 2015. In: Multiple-Point Geostatistics: Stochastic Modeling with Training Images. John Wiley & Sons Ltd, Chichester. https://doi.org/10.1002/9781118662953.

Mariethoz, G., Renard, P., Straubhaar, J., 2010. The Direct Sampling method to perform multiple-point geostatistical simulations. Water Resour. Res. 46 https://doi.org/10.1029/2008WR007621.

Mariethoz, G., 2018. When Should We Use Multiple-Point Geostatistics?, Handbook of Mathematical Geosciences: Fifty Years of Iamg. Springer International Publishing Ag, Cham. https://doi.org/10.1007/978-3-319-78999-6_31.

Marra, F., Morin, E., 2018. Autocorrelation structure of convective rainfall in semiarid-arid climate derived from high-resolution X-Band radar estimates. Atmospheric Res. 200, 126–138. https://doi.org/10.1016/j.atmosres.2017.09.020.

Marra, F., Morin, E., Peleg, N., Mei, Y., Anagnostou, E.N., 2017. Intensity-duration-frequency curves from remote sensing rainfall estimates: Comparing satellite and weather radar over the eastern Mediterranean. Hydrol. Earth Syst. Sci. 21, 2389–2404. https://doi.org/10.5194/hess-21-2389-2017.

Molter, E.M., Collins, W.D., Risser, M.D., 2021. Quantitative precipitation estimation of extremes in CONUS with radar data. Geophys. Res. Lett. 48 https://doi.org/10.1029/2021GL094697.

Moraga, J.S., Peleg, N., Fatichi, S., Molnar, P., Burlando, P., 2021. Revealing the impacts of climate change on mountainous catchments through high-resolution modelling. J. Hydrol. 603, 126806 https://doi.org/10.1016/j.jhydrol.2021.126806.

Muñoz, C., Wang, L.-P., Willems, P., 2018. Enhanced object-based tracking algorithm for convective rain storms and cells. Atmospheric Res. 201, 144–158. https://doi.org/10.1016/j.atmosres.2017.10.027.

Ochoa-Rodriguez, S., Wang, L.-P., Gires, A., Pina, R.D., Reinoso-Rondinel, R., Bruni, G., Ichiba, A., Gaitan, S., Cristiano, E., van Assel, J., Kroll, S., Murlà-Tuyls, D., Tisserand, B., Schertzer, D., Tchiguirinskaia, I., Onof, C., Willems, P., ten Veldhuis, M.-C., 2015. Impact of spatial and temporal resolution of rainfall inputs on urban hydrodynamic modelling outputs: A multi-catchment investigation. J. Hydrol Hydrol. Appl. Weather Radar 531, 389–407. https://doi.org/10.1016/j.jhydrol.2015.05.035.

Oliver, M.A., Webster, R., 2014. A tutorial guide to geostatistics: Computing and modelling variograms and kriging. CATENA 113, 56–69. https://doi.org/10.1016/j.catena.2013.09.006.

Oriani, F., Straubhaar, J., Renard, P., Mariethoz, G., 2014. Simulation of rainfall time series from different climatic regions using the direct sampling technique. Hydrol. Earth Syst. Sci. 18, 3015–3031. https://doi.org/10.5194/hess-18-3015-2014.

Oriani, F., Ohana-Levi, N., Marra, F., Straubhaar, J., Mariethoz, G., Renard, P., Karnieli, A., Morin, E., 2017. Simulating small-scale rainfall fields conditioned by weather state and elevation: A data-driven approach based on rainfall radar images. Water Resour. Res. 53 https://doi.org/10.1002/2017WR020876.

Pavlovic, S., Perica, S., St Laurent, M., Mejia, A., 2016. Intercomparison of selected fixed-area areal reduction factor methods. J. Hydrol. 537, 419–430. https://doi.org/10.1016/j.jhydrol.2016.03.027.

Peleg, N., Blumensaat, F., Molnar, P., Fatichi, S., Burlando, P., 2017. Partitioning the impacts of spatial and climatological rainfall variability in urban drainage modeling. Hydrol. Earth Syst. Sci. 21, 1559–1572. https://doi.org/10.5194/hess-21-1559-2017.

Peleg, N., Marra, F., Fatichi, S., Paschalis, A., Molnar, P., Burlando, P., 2018. Spatial variability of extreme rainfall at radar subpixel scale. J. Hydrol. 556, 922–933. https://doi.org/10.1016/j.jhydrol.2016.05.033.

Peleg, N., Morin, E., 2012. Convective rain cells: Radar-derived spatiotemporal characteristics and synoptic patterns over the eastern Mediterranean. J. Geophys. Res.-Atmospheres 117, D15116. https://doi.org/10.1029/2011JD017353.

Peleg, N., Sinclair, S., Fatichi, S., Burlando, P., 2020. Downscaling climate projections over large and data sparse regions: Methodological application in the Zambezi River Basin. Int. J. Climatol. 40, 6242–6264. https://doi.org/10.1002/joc.6578.

Roe, G.H., 2005. Orographic precipitation. Annu. Rev. Earth Planet. Sci. 33, 645–671. https://doi.org/10.1146/annurev.earth.33.092203.122541.

Schleiss, M., Jaffrain, J., Berne, A., 2012. Stochastic simulation of intermittent DSD fields in time. J. Hydrometeorol. 13, 621–637. https://doi.org/10.1175/JHM-D-11-018.1.

Shen, Y., Hong, Z., Pan, Y., Yu, J., Maguire, L., 2018. China's 1 km merged gauge, radar and satellite experimental precipitation dataset. Remote Sens. 10, 264. https://doi.org/10.3390/rs10020264.

Singhal, A., Jha, S.K., 2022. An application of multiple-point statistics downscaling approach over North-West Himalayas in avalanche-prone areas. Int. J. Climatol. 42, 1902–1921. https://doi.org/10.1002/joc.7342.

Sivapalan, M., Bloschl, G., 1998. Transformation of point rainfall to areal rainfall: Intensity-duration frequency curves. J. Hydrol. 204, 150–167. https://doi.org/10.1016/S0022-1694(97)00117-0.

Sorooshian, S., Hsu, K.-L., Gao, X., Gupta, H.V., Imam, B., Braithwaite, D., 2000. Evaluation of PERSIANN system satellite-based estimates of tropical rainfall. Bull. Am. Meteorol. Soc. 81, 2035–2046.

Thorndahl, S., Nielsen, J.E., Rasmussen, M.R., 2019. Estimation of storm-centred areal reduction factors from radar rainfall for design in urban hydrology. Water 11. https://doi.org/10.3390/w11061120.

Ulbrich, C.W., 1983. Natural variations in the analytical form of the raindrop size distribution. J. Clim. Appl. Meteorol. 22, 1764–1775.

Wang, J., Chen, F., Doan, Q.-V., Xu, Y., 2021. Exploring the effect of urbanization on hourly extreme rainfall over Yangtze River Delta of China. Urban Clim. 36, 100781 https://doi.org/10.1016/j.uclim.2021.100781.

Wright, D.B., Smith, J.A., Villarini, G., Baeck, M.L., 2013. Estimating the frequency of extreme rainfall using weather radar and stochastic storm transposition. J. Hydrol. 488, 150–165. https://doi.org/10.1016/j.jhydrol.2013.03.003.

Xie, P., Joyce, R., Wu, S., Yoo, S.-H., Yarosh, Y., Sun, F., Lin, R., 2017. Reprocessed, bias-corrected CMORPH global high-resolution precipitation estimates from 1998. J. Hydrometeorol. 18, 1617–1641. https://doi.org/10.1175/JHM-D-16-0168.1.

Xing, Y., Ni, G., Yang, L., Yang, Y., Xing, P., Sun, T., 2019. Modeling the impacts of urbanization and open water surface on heavy convective rainfall: A case study over the emerging Xiong'an City, China. J. Geophys. Res.-Atmospheres 124, 9078–9098. https://doi.org/10.1029/2019JD030359.

Yang, P., Ren, G., Yan, P., 2017. Evidence for a strong association of short-duration intense rainfall with urbanization in the Beijing Urban Area. J. Clim. 30, 5851–5870. https://doi.org/10.1175/JCLI-D-16-0671.1.

Yang, L., Tian, F., Smith, J.A., Hu, H., 2014. Urban signatures in the spatial clustering of summer heavy rainfall events over the Beijing metropolitan region. J. Geophys. Res. Atmospheres 119, 1203–1217. https://doi.org/10.1002/2013JD020762.

Yin, S., Li, W., Chen, D., Jeong, J.H., Guo, W., 2011. Diurnal variations of summer precipitation in the Beijing area and the possible effect of topography and urbanization. Adv. Atmospheric Sci. 28, 725–734. https://doi.org/10.1007/s00376-010-9240-y.

Yin, Z., Zuo, C., MacKie, E.J., Caers, J., 2022. Mapping high-resolution basal topography of West Antarctica from radar data using non-stationary multiple-point geostatistics (MPS-BedMappingV1). Geosci. Model Dev. 15, 1477–1497. https://doi.org/10.5194/gmd-15-1477-2022.

Yue, S., Ouarda, T., Bobee, B., 2001. A review of bivariate gamma distributions for hydrological application. J. Hydrol. 246, 1–18. https://doi.org/10.1016/S0022-1694(01)00374-2.

Zhai, Y., Guo, Y., Zhou, J., Guo, N., Wang, J., Teng, Y., 2014. The spatio-temporal variability of annual precipitation and its local impact factors during 1724–2010 in Beijing, China. Hydrol. Process. 28, 2192–2201. https://doi.org/10.1002/hyp.9772.

Zhang, D.-L., 2020. Rapid urbanization and more extreme rainfall events. Sci. Bull. 65, 516–518. https://doi.org/10.1016/j.scib.2020.02.002.

Zhang, X., Zwiers, F.W., Li, G., Wan, H., Cannon, A.J., 2017. Complexity in estimating past and future extreme short-duration rainfall. Nat. Geosci. 10, 255–259. https://doi.org/10.1038/ngeo2911.

Zhu, Z., Wright, D.B., Yu, G., 2018. The impact of rainfall space-time structure in flood frequency analysis. Water Resour. Res. 54, 8983–8998. https://doi.org/10.1029/2018WR023550.

Zou, W., Yin, S., Wang, W., 2021. Spatial interpolation of the extreme hourly precipitation at different return levels in the Haihe River basin. J. Hydrol. 598, 126273 https://doi.org/10.1016/j.jhydrol.2021.126273.